ACS NANO
Cite This: ACS Nano 2018, 12, 2610–2622
www.acsnano.org

ARTICLE

Organic Semiconducting Photoacoustic Nanodroplets for Laser-Activatable Ultrasound Imaging and Combinational Cancer Therapy

Wei Tang,[†] Zhen Yang,[*,†] Sheng Wang,[†] Zhantong Wang,[†] Jibin Song,[†] Guocan Yu,[†] Wenpei Fan,[†] Yunlu Dai,[†] Jingjing Wang,[†] Lingling Shan,[†] Gang Niu,[†] Quli Fan,[*,‡] and Xiaoyuan Chen[*,†]

[†]Laboratory of Molecular Imaging and Nanomedicine (LOMIN), National Institute of Biomedical Imaging and Bioengineering (NIBIB), National Institutes of Health (NIH), Bethesda, Maryland 20892, United States

[‡]Key Laboratory for Organic Electronics and Information Displays & Institute of Advanced Materials (IAM), Jiangsu National Synergetic Innovation Center for Advanced Materials (SICAM), Nanjing University of Posts & Telecommunications, Nanjing 210023, China

Supporting Information

ABSTRACT: **Combination of photoacoustic (PA) and ultrasound (US) imaging offers high spatial resolution images with deep tissue penetration, which shows great potential in applications in medical imaging. Development of PA/US dual-contrast agents with high contrast and excellent biocompatibility is of great interest. Herein, an organic semiconducting photoacoustic nanodroplet, PS-PDI-PAnD, is developed by stabilizing low-boiling-point perfluorocarbon (PFC) droplet with a photoabsorber and photoacoustic agent of perylene diimide (PDI) molecules and coencapsulating the droplet with photosensitizers of $ZnF_{16}Pc$ molecules. Upon irradiation, the PDI acts as an efficient photoabsorber to trigger the liquid-to-gas phase transition of the PFC, resulting in dual-modal PA/US imaging contrast as well as photothermal heating. On the other hand, PFC can serve as an O_2 reservoir to overcome the hypoxia-associated resistance in cancer therapies, especially in photodynamic therapy. The encapsulated photosensitizers will benefit from the sustained oxygen release from the PFC, leading to promoted photodynamic efficacy regardless of pre-existing hypoxia in the tumors. When intravenously injected into tumor-bearing mice, the PS-PDI-PAnDs show a high tumor accumulation *via* EPR effect. With a single 671 nm laser irradiation, the PS-PDI-PAnDs exhibit a dual-modal PA/US imaging-guided synergistic photothermal and oxygen self-enriched photodynamic treatment, resulting in complete tumor eradication and minimal side effects. The PS-PDI-PAnDs represents a type of PFC nanodroplets for synergistic PDT/PTT treatment upon a single laser irradiation, which is expected to hold great potential in the clinical translation in dual-modal PA/US imaging-guided combinational cancer therapy.**

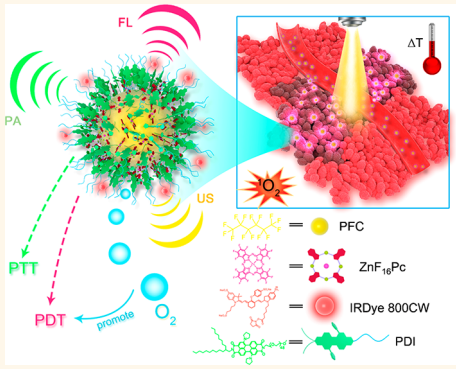

KEYWORDS: *organic semiconducting nanodroplets, photoacoustic imaging, ultrasound imaging, photothermal therapy, oxygen self-enriched photodynamic therapy*

Ultrasound (US) imaging is one of the most frequently used imaging modalities in clinics owing to its noninvasion, nonionization, deep tissue penetration, and relatively low cost.[1−3] Recently, phase-changeable perfluorocarbon (PFC) nanodroplets have been investigated as an alternative US contrast agent due to their excellent colloidal stability, prolonged circulation time, and efficient tumor vascular permeability.[1,4−6] They are stabilized by a shell of protein,[4,7] lipids,[8−10] polymers,[1,11] or inorganic nanoparticles[12,13] and have poor echogenic sensitivity at body temperature (37 °C). However, the low-boiling-point PFC nanodroplets allow vaporization by thermal effects, resulting in bubbles for enhanced US contrast. Laser and acoustic irradiation are the two most used external stimulus strategies to vaporize PFC nanodroplets.[6,14] While an acoustic droplet vaporization (ADV) event often requires acoustic pressures and frequencies that may cause unwanted bioeffects,[15,16] an optical droplet vaporization (ODV) process is safer and more controllable.[4,17] Moreover, the photoabsorbers for ODV process are usually supplemented with photoacoustic (PA) contrast,[4,5] making the nanodroplets eligible for dual-modal PA/US imaging, which offers high spatial resolution images

Received: December 5, 2017
Accepted: February 16, 2018
Published: February 16, 2018

DOI: 10.1021/acsnano.7b08628
ACS Nano 2018, 12, 2610–2622

with deep tissue penetration. A variety of photoabsorbers can be integrated into the PFC nanodroplets, ranging from inorganic nanoparticles (*i.e.*, gold nanorods,[4,18] PbS nanoparticles,[19] CuS nanoparticles[5]) to organic molecules (*i.e.*, ICG[17] and porphyrin[14]). Although they have shown great potential in dual-modal PA/US imaging applications, these formulations have struggled to be used in the clinic. For example, gold nanorods are neither biodegradable nor effectively cleared,[20,21] which raises long-term toxicity and safety concerns. Besides, gold nanorods may easily get melted and shape-changed upon laser irradiation,[22] altering the absorbance peak, thus lowering the photothermal conversion efficiency at the preset irradiation wavelength. ICG, for another example, is susceptible to photobleaching and leads to limited long-term applications.[17] Therefore, a photoabsorber with good photothermal stability and efficiency, effective PA performance, as well as excellent biocompatibility is highly desired.

Semiconducting organic molecules,[23−28] such as perylene diimide (PDI),[29−31] has attracted great interest in PA imaging due to its strong near-infrared (NIR) light absorption and excellent biocompatibility. Moreover, PDI possesses exceptional high photothermal stability and efficiency, easy modification, strong intramolecular $\pi-\pi$ stacking for self-assembly, and extremely low cost.[29,31] All these properties grant PDI an ideal photoabsorber candidate in the laser-activatable PFC nanodroplets for tumor US/PA imaging. The PFC nanodroplets, on the other hand, can act as an oxygen reservoir to efficiently promote tumor oxygenation and overcome the hypoxia-associated resistance in cancer therapies, especially in radiotherapy and photodynamic therapy (PDT).[7,32−34] Specifically, PFC has an extremely high oxygen solubility,[35−37] proving sustained oxygen diffusion in hypoxia environment through the oxygen concentration gradient. During PDT, for instance, the oxygen self-enriched PFC core can afford sufficient oxygen for photosensitizers (PSs) to consume, continuously generate cytotoxic $^1O_2$, thus achieving improved PDT efficacy regardless of pre-existing hypoxia in the tumors. If PSs with similar absorbance peak of the PDI molecules were encapsulated into the PFC nanodroplets, a simultaneously photothermal therapy (PTT) and oxygen self-enriched PDT (Oxy-PDT) could be achieved upon a single laser irradiation, which could expect synergistic therapeutic efficacies to significantly inhibit the tumor growth and kill cancer.[38]

Herein, we have developed a PS-loaded PDI photoacoustic nanodroplet (PS-PDI-PAnD) *via* a simple one-step nanoprecipitation process. The resulting PS-PDI-PAnD consists of a liquid perfluoropentane (bp = 29 °C) core, a PDI shell, and uniformly dispersed PSs—Zinc 1,2,3,4,8,9,10,11,15,16,17,18,22,23,24,25-hexadecafluoro-29*H*,31*H*-phthalocyanine molecules ($ZnF_{16}Pc$, $\lambda_{max} \approx 671$ nm, $\Phi_\Delta = 0.85$ in THF[39]) at the interface of the core−shell structure (Scheme 1). Unlike other photoabsorbers that either suspended in the PFC core[4,5] or coated on the surface of the stabilizing shell,[40] the semiconducting amphiphilic PDI molecules (Figure S1) served as a stabilizing shell of the nanodroplets due to their strong $\pi-\pi$ stacking and the long alky chains. $ZnF_{16}Pc$ molecules were used as PSs because they are high potent and their intrinsic 16 fluorine atoms make them well compatible with PFC. When irradiated the PS-PDI-PAnDs with a 671 nm laser light, the PDI shell would convert light energy into heat, trigger the liquid-to-gas phase conversion of the PFC core for contrast-enhanced US imaging, as well as induce the photothermal killing effect; the encapsulated PSs would benefit from the continuous O_2 release from the PFC core, resulting in promoted $^1O_2$ generation for Oxy-PDT. It is worth noting that the photothermal effect can accelerate the tumor blood flow, widen the endothelial gaps, enhance the permeability of cancer cell membranes, and increase the O_2 release from PFC,[38] thus improving the delivery of the PS-PDI-PAnDs together with O_2 and subsequently promoting intracellular $^1O_2$ generation. Moreover, as more PFC are vaporized, there may be a cavitation effect[6] and a burst release of O_2,[41] which strongly disturb the tumor structure for deep penetration of the therapeutic agents,[6,42,43] and instantly oxygenate the whole tumor[41] to further promote the PDT effect. Therefore, the PS-PDI-PAnDs will demonstrate a dual-modal PA/US imaging guided synergistical PTT/Oxy-PDT (Scheme 1). In this study, we first assessed the PA and US contrast ability of the PS-PDI-PAnDs both *in vitro* and *in vivo*. Next, we compared the photodynamic effect between Oxy-PDT and conventional PDT. Last, we investigated the treatment efficacy of the combinational PTT and Oxy-PDT against cancer. It is expected that the PS-PDI-PAnDs holds great potentials in the clinical translation in multimodal imaging guided combinational cancer treatment.

Scheme 1. IRDye800CW-Labeled Photosensitizer $ZnF_{16}Pc$-Loaded PDI Photoacoustic Nanodroplet (PS-PDI-PAnD) for *In Vivo* Multimodal Imaging Guided Combinational Photothermal and Oxygen Self-Enriched Photodynamic Therapy[a]

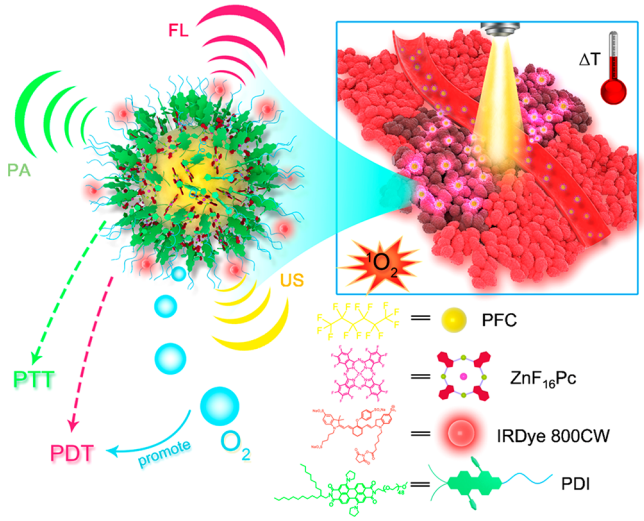

[a]When irradiated the PS-PDI-PAnDs with a 671 nm laser, the PDI shell will convert light energy into heat, vaporize the PFC core for contrast-enhanced US imaging, as well as kill cancerous cells by photothermal effect. Meanwhile, the encapsulated PSs will transfer light energy to the oxygen, benefiting from the sustained O_2 release from the PFC core, resulting in promoted $^1O_2$ generation and enhanced PDT effect.

RESULTS AND DISCUSSION

Preparation of the PS-PDI-PAnDs. The PS-PDI-PAnDs were prepared by following our published protocols with slight modifications.[31] Two asymmetric amphiphilic PDI structures, PEG-based PDI (Structure 1, Figure S1) and amine functional PEG-based PDI (Structure 2, Figure S1), were synthesized and dissolved in tetrahydrofuran (THF) at a molar ratio of 9:1. Then, $ZnF_{16}Pc$ molecules and perfluoropentane were added.

DOI: 10.1021/acsnano.7b08628
ACS Nano 2018, 12, 2610−2622

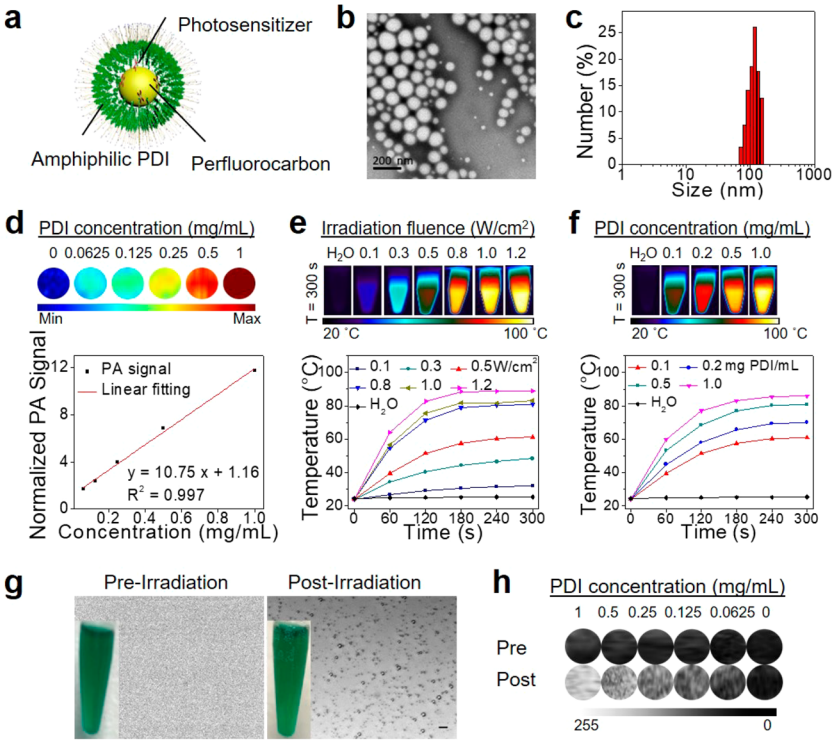

Figure 1. Characterization of the PS-PDI-PAnDs. (a) Structure and design of the PS-PDI-PAnDs. PSs and PFC were coencapsulated by the self-assembled amphiphilic PDI molecules. The PSs were uniformly dispersed at the interface of the PDI shell and PFC core. (b) TEM image showed a uniformly distributed core−shell structure. (c) Dynamic light scattering analysis indicated a diameter of 113.5 ± 24.2 nm. (d) PA images and signals of PS-PDI-PAnDs as a function of concentration. (e) Photothermal heating images and curves of PS-PDI-PAnDs aqueous solution (0.1 mg PDI/mL) with different laser irradiation fluence. (f) Photothermal heating images and curves of PS-PDI-PAnDs aqueous solution at different concentrations with a 0.5 W/cm² laser irradiation. (g) Optical images of the PS-PDI-PAnDs before and after laser irradiation. Scale bar, 20 μm. Inserted images, PS-PDI-PAnDs soulution irradiated in a PE tube. (h) B-mode US images of the PS-PDI-PAnDs at different concentrations before and after the laser irradiation.

The mixture was subjected to a brief sonication and was dropwise added with 1 mL of H_2O under rapid stirring. Finally, the PS-PDI-PAnDs were acquired after a slow and complete vaporization of THF. The loading ratio of $ZnF_{16}Pc$ molecules was determined through UV−vis spectroscopy (Figure S2) by comparing unloaded $ZnF_{16}Pc$ molecules to a pre-established standard curve. A formulation with a PDI to $ZnF_{16}Pc$ molar ratio of around 10:1 was used for subsequent studies. Transmission electron microscopy (TEM, Figure 1b) analysis demonstrated a uniformly distributed core−shell structure of the resulting PS-PDI-PAnDs. An average hydrodynamic size of 113.5 ± 24.2 nm was measured by dynamic light scattering (DLS, Figure 1c), which result was well corroborated with the TEM observations. The PS-PDI-PAnDs showed excellent colloidal stability (Figure S3). Their particle size kept stable after 3 days incubation in different media (*i.e.*, H_2O, PBS, 10% FBS, and DMEM) at different temperature conditions (*i.e.*, 4, 29, 37 °C). The good stability was attributed to the PDI stabilizing shell, which dramatically lowered the surface tension, prevented droplet coalescence, therefore preventing premature vaporization of PFP even at temperature (37 °C) higher than its boiling point (29 °C).[1,4,7] In comparison, $ZnF_{16}Pc$-loaded PDI nanoparticles (PS-PDI-PAnPs) and PDI nanoparticles (PDI-PAnPs) were prepared. The initial concentrations of PDI and $ZnF_{16}Pc$ were carefully adjusted to achieve the same $ZnF_{16}Pc$ loading ratio and similar particle sizes with the nanodroplets. Without adding PFC, uniform solid particle structures at diameters of around 100 nm were observed under TEM (Figure S4a). DLS indicated consistent results with the TEM analysis, showing average diameters of 108.1 ± 13.6 and 106.8 ± 12.7 nm for the PS-PDI-PAnPs and PDI-PAnPs, respectively (Figure S4b). The absorbance spectra (Figure S5) of PS-PDI-PAnDs and PS-PDI-PAnPs indicated a slight blue shift of the characteristic H-aggregate band of the PDI-PAnPs at ~650 nm,[31] suggesting the successful loading of the $ZnF_{16}Pc$ molecules. Moreover, the PS-PDI-PAnDs showed a shaper peak than the PS-PDI-PAnPs, which may due to less aggregation of $ZnF_{16}Pc$ molecules in the nanodroplets. On the basis of the $ZnF_{16}Pc$ structure, we postulated that the intrinsic 16 fluorine atoms in the molecule may facilitate their dissolving in the PFC, inhibit intermolecular $\pi-\pi$ stacking of the PSs, and lead to uniform distribution at the interface of the PDI and the PFC. In addition, a number of amine groups were displayed on the nanodroplet surfaces, which can be used for radiolabeling,[31] dye labeling,[44] and targeting motif conjugation.[45] In this study, we labeled the nanodroplets with IRDye800 for *in vivo* optical imaging.

***In Vitro* Photoacoustic, Photothermal, and Ultrasound Properties of the PS-PDI-PAnDs.** The PDI was demonstrated to be an effective photoabsorber and PA contrast agent.[30,31] To investigate the PA properties of PS-PDI-PAnDs, their solutions at concentrations ranging from 0.0625 to 1 mg PDI/mL were filled into different capillaries. The capillaries were then immersed in a homemade water tank and measured under a Visual Sonic Vevo 2100 LAZR system. Figure 1d revealed that the PA signal intensity was a function of the

DOI: 10.1021/acsnano.7b08628
ACS Nano 2018, 12, 2610−2622

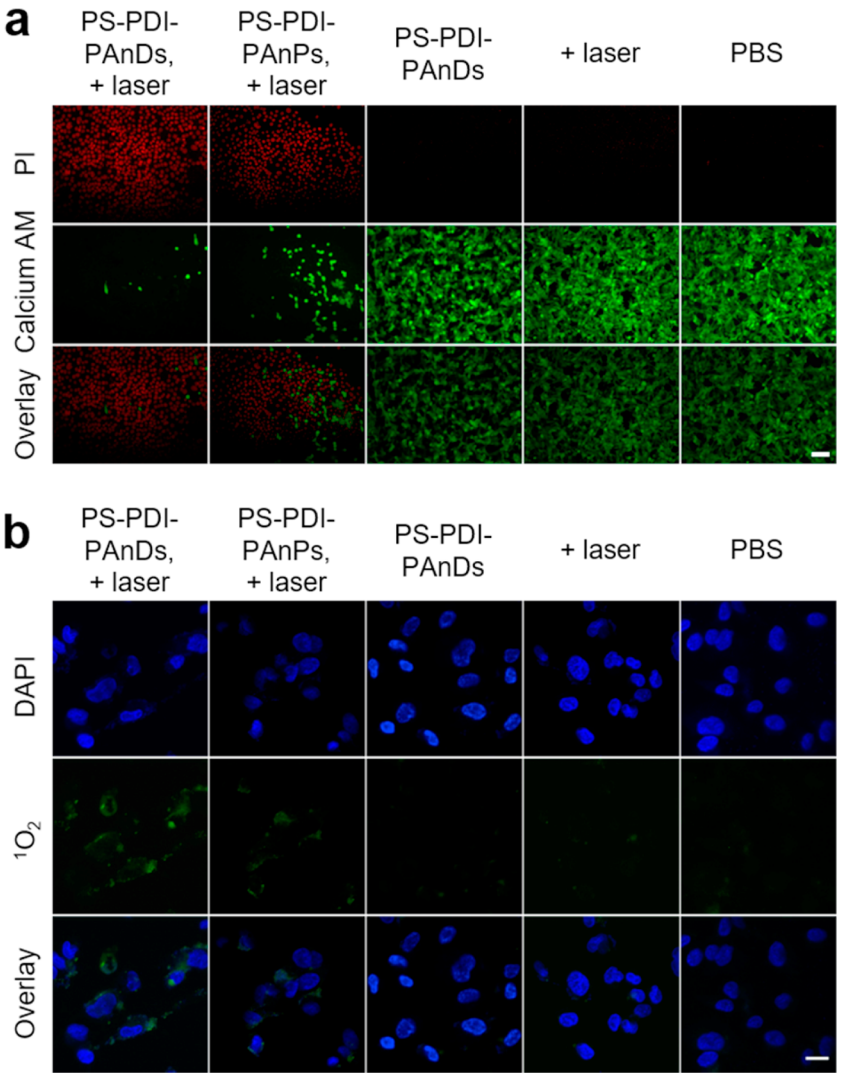

Figure 2. ***In vitro*** **Oxy-PDT with U87MG cells. Cells were coincubated with the PS-PDI-PAnDs for 24 h before a laser irradiation applied (671 nm, 0.1 W/cm^2, 200 s). Cells treated with PS-PDI-PAnPs at the same PDI concentration and exposed to the same laser irradiation were performed as conventional PDT control. For other controls, cells were treated with PS-PDI-PAnDs only, laser only, or PBS only. (a) Live and dead assays conducted 24-h after the treatment. Live cells, Calcium AM, green fluorescence. Dead cells, PI, red fluorescence. Wide spread cell death was observed in both Oxy-PDT and PDT treated groups, where Oxy-PDT demonstrated a significantly better cell killing efficacy. In contrast, extensive live cells were found in the other controls. Scale bar, 100 μm. (b) $^1O_2$ generation right after the treatment. The Oxy-PDT group showed a significantly higher level of $^1O_2$ signals than that of the PDT-treated group. Marginal $^1O_2$ signals were detected in the other three control groups. Scale bar, 20 μm.**

concentration of PDI molecules. The corresponding quantitative analysis of the PA signals showed a linearly positive correlation with PDI concentration (R^2 = 0.997, Figure 1d). The observed strong PA signals were attributed to thermal expansion, which is the only biologically safe mechanism of the PA imaging to date.[4] Specifically, the PS-PDI-PAnDs absorbed the short laser pulses from the LAZR system, causing localized volume heating, resulting in rapid expansion and generation of acoustic pressure waves. In addition, the PA performance of the PS-PDI-PAnDs were in good correspondence with that of our previously reported 100 nm-sized PDI-PAnPs,[31] indicating that the PFC and PS encapsulation did not comprise the PA performance of the PDI components. All these results suggested the PS-PDI-PAnDs a safe and efficient PA imaging probe.

To evaluate the photothermal conversion capacity of the PS-PDI-PAnDs, we irradiated PS-PDI-PAnD solutions (0.1 mg PDI/mL) with a 671 nm laser at different irradiation fluence (0.1, 0.3, 0.5, 0.8, 1.0, 1.2 W/cm^2) for 5 min. The temperature changes were recorded with an infrared (IR) camera and were plotted over the irradiation time in Figure 1e. Increased temperature rise was observed with increasing irradiation fluence. As the irradiation fluence raising from 0.1 to 1 W/cm^2, the temperature of the solutions was rapidly increased to 26.6, 34.2, 39.3, 54.4, 56.5, and 63.9 °C in 1 min. At the end of the 5 min irradiation, the solutions were heated to 32.0, 48.3, 61.0, 80.9, 83.1, and 89.0 °C, respectively. In contrast, deionized water irradiated at 1.2 W/cm^2 found no obvious temperature rise (<1.0 °C) during the irradiation. The IR photographs visualized the same conclusions, displaying an obviously higher temperature with higher irradiation fluence applied (Figure 1e). We also examined the PDI concentration-dependent PTT effect. The PS-PDI-PAnD solutions at concentrations ranging from 0.1 to 1.0 mg PDI/mL were

DOI: 10.1021/acsnano.7b08628
ACS Nano 2018, 12, 2610−2622

exposed to a 671 nm laser at 0.5 W/cm^2 for 5 min. The photothermal heating photographs and curves shown in Figure 1f consolidated our hypothesis, which was higher PDI concentration led to more efficient photothermal conversion. At the end of the irradiation, the solutions were heated to 61.0, 70.1, 80.9, and 85.9 °C, respectively. These results suggested the PS-PDI-PAnDs could promptly and efficiently convert light energy into heat in both an irradiation fluence-dependent and a PDI concentration-dependent manner, implying their potential applications in ODV-induced US imaging.

The nanosized PS-PDI-PAnDs could not effectively respond to US due to their poor echogenic sensitivity. Once the liquid-to-gas phase transition of the PS-PDI-PAnDs was initiated, however, the generated gaseous phase of the PFC would induce a significant acoustic impedance mismatch with the surrounding environment, thus exhibiting enhanced US contrast.[4] Figure 1g confirmed the successful ODV process of the PS-PDI-PAnDs. The PS-PDI-PAnD solution was irradiated with a 671 nm laser (0.5 W/cm^2, 3 min) either on a sealed glass slide or in a PE tube. Large-sized gas bubbles were observed after the photoirradiation in both situations, which may be because of coalescence of several nearby individual microbubbles.[4] Finally, we evaluated the ODV-induced US contrast enhancement of the PS-PDI-PAnDs by comparing their performance in solutions at different concentrations before and after the laser irradiation. Upon irradiation, the US images displayed increased contrast enhancement with increasing concentration of the solutions (Figure 1h). At the concentration of 1 mg PDI/mL, the B-mode contrast increased by 4.2 times (Figure S6a). In comparison, PS-PDI-PAnPs and PDI-PAnPs at the same concentration of 1 mg PDI/mL showed no contrast enhancement after the irradiation (Figure S6b and S6c). Therefore, the ODV of the liquid PFC core provided enhanced US contrast, demonstrating the feasibility of using PS-PDI-PAnDs as a laser-activatable US contrast agent.

***In Vitro* Oxy-PDT Effect with the PS-PDI-PAnDs.** PFC, on the other hand, can act as an adjuvant in PDT due to its high oxygen capacity. Next, we tested the phototoxicity from the Oxy-PDT with PS-PDI-PAnDs with U87MG cells by using 3-(4,5-dimethythiazon-2-yl)-2,5-diphenyl tetrazolium bromide (MTT) assays. The PS-PDI-PAnPs (without PFC loading) were tested as a control of conventional PDT. A low-fluence laser irradiation at 0.1 W/cm^2 was applied in both groups, which fluence was not enough to induce an effective photothermal effect as shown in Figure 1e. Thus, the phototoxicity in this experiment was only from PDT but not PTT. Without laser irradiation, no significant U87MG cell death was observed in both groups at the concentration of 100 μg PDI/mL or below (Figure S7a), indicating good biocompatibility of the nanotheranoastic agents. In addition, the PS-PDI-PAnDs showed excellent biocompatibility to normal cell lines. After 24 h coincubation with the PS-PDI-PAnDs, the cell viability of HUVEC and NIH/3T3 cells remained 88% and 75% at a high concentration of 400 μg PDI/mL, respectively (Figure S8). Upon 200 s of continuous laser irradiation (671 nm, 0.1 W/cm^2), however, concentration-dependent reductions in U87MG cell viability were notably detected (Figure S7b). At the concentration of 100 μg PDI/mL, the cell viability after photoirradiation was 17.12 ± 5.53% and 33.17 ± 4.95% for the PS-PDI-PAnDs and PS-PDI-PAnPs, respectively. The PS-PDI-PAnDs showed significantly lower cell viability than that of PS-PDI-PAnPs at all tested concentrations, suggesting improved PDT efficacy with PFC loading. In addition, cells treated with PDI-PAnPs (without PFC and PSs loading) were also examined to evaluate the impact from the photothermal effect (Figure S7). No substantial differences in cell viability were found before and after the photoirradiation (671 nm, 0.1 W/cm^2, 200 s) at the same PDI concentration, further confirming that the low-fluence irradiation at 0.1 W/cm^2 could not induce effective cell killing *via* the photothermal effect with the PDI components. Therefore, the low-fluence irradiation at 0.1 W/cm^2 only activated the Oxy-PDT effect with the PS-PDI-PAnDs *in vitro*. To verify the Oxy-PDT efficacy, we visualized the cell viability with the live/dead staining (Figure 2a), where live cells stained in green fluorescence with calcium AM and dead cells stained in red with propidium iodide (PI). A significantly higher level of red fluorescence activities was observed in the PS-PDI-PAnDs group than in the PS-PDI-PAnPs group after the photoirradiation (671 nm, 0.1 W/cm^2, 200 s). Meanwhile, control groups of cells treated with PS-PDI-PAnDs alone, photoirradiation alone, or PBS exhibited only widespread green fluorescence but negligible red fluorescence signals, indicating minimal cell damage, which was not surprising because of the absence of PSs and/or photoirradiation. Taken together, both MTT and live/dead assay found more phototoxicity of PS-PDI-PAnDs than PS-PDI-PAnPs. These observations should be attributed to the O_2 self-enriched PFC core, which led to a relatively high local O_2 concentration and therefore more efficient $^1O_2$ production in the Oxy-PDT.

To confirm the promoted $^1O_2$ generation in Oxy-PDT, we used SOSG as a $^1O_2$ marker. Specifically, the PS-PDI-PAnDs and SOSG working solution were injected into a cap-open cuvette that had been preloaded with PBS. Then, a low-fluence laser irradiation (671 nm, 0.1 W/cm^2) was applied, under which circumstance only induced PDT but not PTT effect. The $^1O_2$ production was determined by measuring fluorescence intensity at 525 nm at selected time points. In the control group, conventional PDT with PS-PDI-PAnPs at the same $ZnF_{16}Pc$ concentration and irradiation doses was studied. As shown in Figure S9a, the Oxy-PDT induced a 2.3-time higher $^1O_2$ quantum yield than the conventional PDT due to the high O_2 capacity of the PFC. To better estimate whether O_2 diffusion from the PFC was a key player in the Oxy-PDT, we repeated the experiments in a low oxygen condition. The nanotheranostic agents were injected into a sealed cuvette that had been preloaded with PBS and bubbled with argon gas. Figure S9b indicated little $^1O_2$ production with the PS-PDI-PAnPs, which mainly due to the oxygen-free environment. In sharp contrast, the PS-PDI-PAnDs provided continuous $^1O_2$ generation in the closed system, showing comparable $^1O_2$ quantum yield to that under the normoxia environment (Figure S9). These observations again demonstrated the oxygen self-enriched PFC acted as an O_2 reservoir during the Oxy-PDT, providing sustained O_2 supply for efficient $^1O_2$ generation, even under hypoxia conditions. Moreover, we compared the $^1O_2$ production of Oxy-PDT and conventional PDT on U87MG human glioma cells (Figure 2b). The cells were coincubated with the nanotherapeutic agents for 24 h. After a 671 nm laser irradiation (0.1 W/cm^2, 200 s), the cells treated with PS-PDI-PAnDs showed a significantly higher level of green fluorescence stained with SOSG than the cells treated with PS-PDI-PAnPs, suggesting a significantly higher amount of $^1O_2$ generation in Oxy-PDT. For controls, we treated the cells with PS-PDI-PAnDs only, irradiation only, and PBS. Negligible

DOI: 10.1021/acsnano.7b08628
ACS Nano 2018, 12, 2610−2622

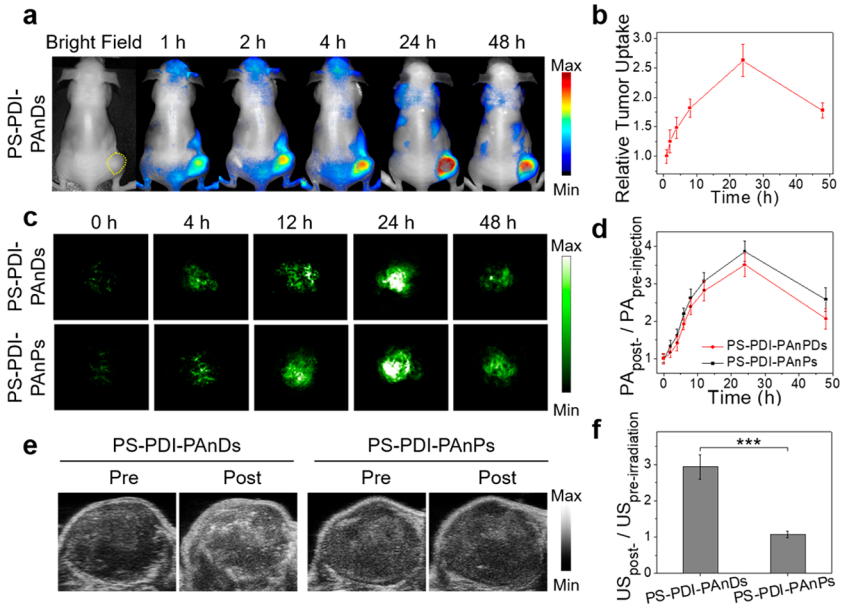

Figure 3. ***In vivo*** **multimodal imaging of the PS-PDI-PAnDs. (a) Representative fluorescence images taken at different time points after the PS-PDI-PAnDs injection (label with IRDye800). Tumors were circled with yellow dashed lines. The PS-PDI-PAnDs gradually accumulated at tumors over time, showing a maximum tumor uptake at 24-h p.i. (b) Quantitative analysis of relative tumor uptake based on (a). (c) PA images and (d) PA signal intensity changes of U87MG tumor-bearing mice pre- and post- i.v. injection of PS-PDI-PAnDs and PS-PDI-PAnPs. The PS-PDI-PAnDs and PS-PDI-PAnPs showed similar tumor accumulation, which may because of their similar particle size and surface chemistry. (e) B-mode US images and (f) relative US signal increase of U87MG tumor-bearing mice before and after photoirradiation. The PS-PDI-PAnDs and PS-PDI-PAnPs were i.v. injected into the mice 24 h before the photoirradiation. After irradiation, significant US contrast enhancement (improved by 2.93 times) was observed in the tumors with the PS-PDI-PAnDs injection, while no detectable US contrast changes were found in the PS-PDI-PAnPs group. ***$P < 0.001$.**

fluorescence signals were detected in all control groups. The observed fluorescence activities were in good accordance with the PI staining in the live/dead assays (Figure 2a), validating that the enhanced cell killing efficacy from Oxy-PDT was benefited from the promoted $^1O_2$ production, which further attributed to the sufficient and sustained O_2 supply from the PFC. We then measured the *in vitro* oxygen release profile of the PS-PDI-PAnDs in a sealed, N_2-filled, and deoxygenated water-loaded tube (Figure S10). The oxygen level rapidly increased and gradually saturated within 5 min, indicating effective oxygen loading and gradual oxygen release. Subsequently, the tube was incubated in a 42 °C water bath and found a burst-like increase in the oxygen concentration, which may due to the PFC vaporization. Therefore, the oxygen release could be controlled by the surrounding temperature. The conclusion was confirmed *in vitro* in hypoxic U87MG cells with an oxygen indicator $[Ru(dpp)_3]Cl_2$ (Figure S11a). In addition, MTT assays on hypoxic U87MG cells found a positive correlation between PDT efficiency and oxygen release rate (Figure S11b). All these data again reinforced the significant contributions of PFC, or the sufficient and sustained oxygen release from the PFC, to the enhancement in the Oxy-PDT treatment efficacy.

In Vivo **Multi-Modal Imaging with the PS-PDI-PAnDs.** We next investigated the *in vivo* multimodal imaging capability of the PS-PDI-PAnDs. Before *in vivo* imaging, the blood circulation and tissue distribution were studied in healthy balb/c mice (Figure S12). Then, the performance of the PS-PDI-PAnDs in near-infrared fluorescence (NIRF) imaging was evaluated by intravenously (i.v.) injecting the PS-PDI-PAnDs (labeled with IRDye800) into U87MG tumor-bearing mice. The PS-PDI-PAnDs were gradually accumulated at the tumors and exhibited the highest tumor accumulation at 24-h postinjection (p.i.) (Figure 3a). According to region of interest (ROI) analysis, the relative tumor uptake of the PS-PDI-PAnDs were 1 ± 0.11, 1.25 ± 0.20, 1.48 ± 0.18, 2.62 ± 0.27 and 1.78 ± 0.13 times at 1, 2, 4, 24, and 48-h p.i., respectively (Figure 3b). After the 48-h imaging, the tumors and major organs were collected for *ex vivo* imaging (Figure S13). High fluorescence intensity was detected in tumors, but low IRDye800 signals were found in the skin, indicating minimal skin toxicity to light exposure, which is a major concern for phototherapies.[46,47] *In vivo* PA performance of the PS-PDI-PAnDs was also evaluated. The PS-PDI-PAnDs were i.v. injected into the mice and the tumors were imaged (Figure 3c). The PA signal intensity changes at tumor regions were consistent with the NIRF imaging results, showing gradually increase at early time points and the maximum accumulation at 24-h p.i. By quantitative analysis, the PA signals at tumors were enhanced by 1.41 ± 0.20, 2.81 ± 0.27, 3.51 ± 0.31, and 2.06 ± 0.28 folds at 4, 12, 24, 48-h p.i., respectively (Figure 3d). The *ex vivo* PA imaging on tumor and major organs at 48-h p.i. showed similar results as the NIRF imaging (Figure S14). As a comparison, the PS-PDI-PAnPs were injected. Similar tumor accumulation profile was observed as that of the PS-PDI-PAnDs (Figure 3c and 3d), which may because of their similar size and surface chemistry. Furthermore, we investigated the ODV-induced US contrast enhancement of the PS-PDI-PAnDs. On the basis of the NIRF and PA imaging results, a 671 nm laser was irradiated at the tumors (671 nm, 0.5 W/cm^2, 3 min) at 24-h p.i. of the PS-PDI-PAnDs. US images of tumors were acquired before and after the photoirradiation (Figure 3e). At the end of the photoirradiation, the B-mode contrast of the tumors was increased by 2.93 times (Figure 3f). In contrast, mice injected with PS-PDI-

DOI: 10.1021/acsnano.7b08628
ACS Nano 2018, 12, 2610−2622

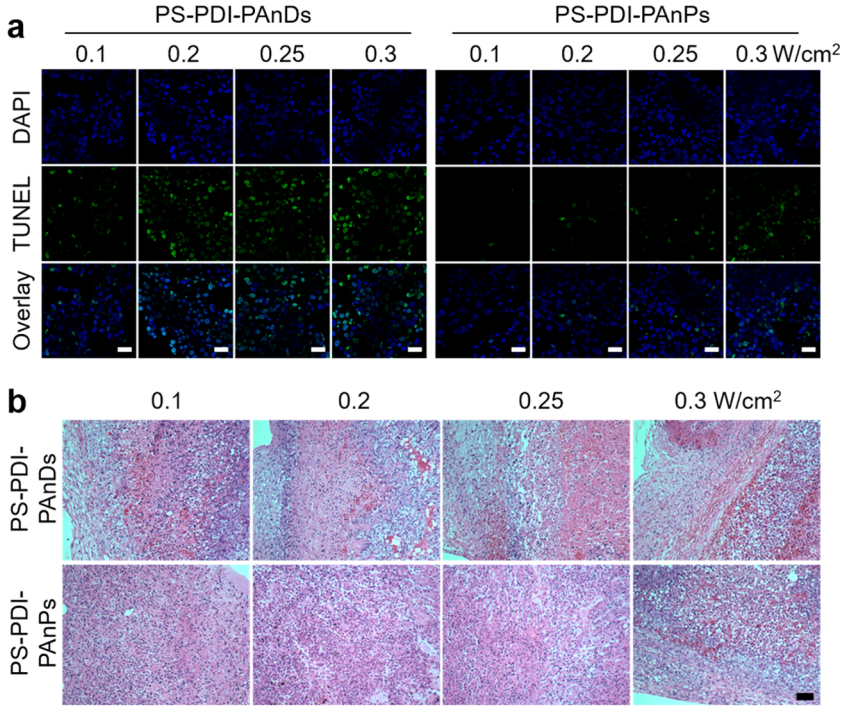

Figure 4. ***In vivo*** **Oxy-PDT with PS-PDI-PAnDs. PS-PDI-PAnDs were i.v. injected into U87MG tumor-bearing mice. A 671 nm laser was subsequently applied to the tumors for 10 min at different irradiation fluence. Conventional PDT with PS-PDI-PAnPs were investigated as controls. (a) TUNEL assay (Green, TUNEL. Blue, DAPI. Scale bar, 20 μm) and (b) H&E staining (Scale bar, 100 μm) results, performed on tumor samples acquired 24-h after the PDT. Oxy-PDT showed significantly improved efficacy than conventional PDT at all irradiation fluences tested. An irradiation fluence-dependent PDT effect was observed in the Oxy-PDT treatment. There was a large difference in Oxy-PDT efficacy between 0.2 and 0.1 W/cm^2 treated animals; however, further increasing the irradiation fluence induced no significant improvement in efficacy.**

PAnPs displayed no obvious differences in the US images (Figure 3e and 3f). These results evidenced the PDI components as excellent photoabsorbers to facilitate the vaporization of PFC for ultrasound detection. In summary, the PS-PDI-PAnDs were demonstrated to be an effective and efficient NIRF/PA/US multimodal imaging agent.

In Vivo **Oxy-PDT Effect with the PS-PDI-PAnDs.** Inspired by the efficient tumor accumulation of the nano-theranostic agents, we evaluated the Oxy-PDT *in vivo* by comparing the treatment efficacy between PS-PDI-PAnDs and PS-PDI-PAnPs on a mice U87MG tumor model. As the irradiation fluence is an important parameter for PDT,[44] we assessed the efficacy in a fluence-dependent manner. Briefly, we inoculated U87MG cells to the right hind leg of nude mice. When the tumors reached a size of 200 mm^3, we intravenously injected the mice (n = 3) with PS-PDI-PAnDs or PS-PDI-PAnPs (200 μL of 5 mg PDI/mL) and irradiated the tumors at 24-h p.i. The irradiation time was maintained 10 min, but the irradiation fluence was elevated from 0.1 to 0.3 W/cm^2. During the irradiation, the local tumor temperature was monitored and recorded (Figure S15). 24 h after the PDT treatment, we euthanized the animals and collected the tumor tissues for terminal deoxynucleotidyl transferase dUTP nick end labeling (TUNEL) assays (Figure 4a) as well as hematoxylin and eosin (H&E) staining (Figure 4b).

The TUNEL assays showed an obvious dose-dependent treatment efficacy in the Oxy-PDT with PS-PDI-PAnDs. While moderate levels of positive fluorescence signals were detected at 0.1 W/cm^2, extensive apoptotic cells were found when the irradiation fluence was increased to 0.2 W/cm^2 or above (Figure 4a). The H&E staining demonstrated similar results as the TUNEL staining, showing large areas of necrosis and bleeding in the tumors with irradiation fluences at 0.2 W/cm^2. Further increasing the irradiation fluence to 0.25 and 0.3 W/cm^2 showed marginal differences in the efficacy of the Oxy-PDT treatment (Figure 4b). Conventional PDT with the PS-PDI-PAnPs, however, only detected cancer cell killing effect at the highest irradiation fluence of 0.3 W/cm^2, suggesting a less effective efficacy than Oxy-PDT. To assess the tumor killing resulted from the PTT effect, we monitored the temperature of the tumor regions during the laser irradiation. At all irradiation fluences, the tumor temperatures were not exceeded to 41 °C (Figure S15), which was not enough to induce thermal ablation at tumors. Therefore, the observed tumor damages were only induced by PDT effect, but not PTT. All these results further confirmed the O_2 self-enriched PFC played an important role in promoting the treatment efficacy of the Oxy-PDT.

To visualize the tumor oxygenation during the Oxy-PDT, PA images of the oxygenated hemoglobin (λ = 850 nm) in tumors were recorded (Figure S16a) and quantified (Figure S16b). At 24 h p.i. of the PS-PDI-PAnDs, the PA signals were increased by ~1.9 times, suggesting enhanced tumor oxygenation, which was attributed to the gradual and sustained oxygen release from the encapsulated PFC. Moreover, a subsequent irradiation (671 nm, 0.2 W/cm^2, 10 min) did not lower the tumor oxygen level, consolidating the sustained oxygen release. In contrast, administration of PS-PDI-PAnPs failed to alleviate the tumor hypoxia at 24 h p.i., and the following laser irradiation further dropped the tumor oxygen level by ~20%. After 30 min of the irradiation, the tumors were collected for hypoxia-inducible factor 1-α (HIF1-α) staining (Figure S16c), which displayed strong positive HIF-1α signals in the PS-PDI-PAnP-treated

DOI: 10.1021/acsnano.7b08628
ACS Nano 2018, 12, 2610−2622

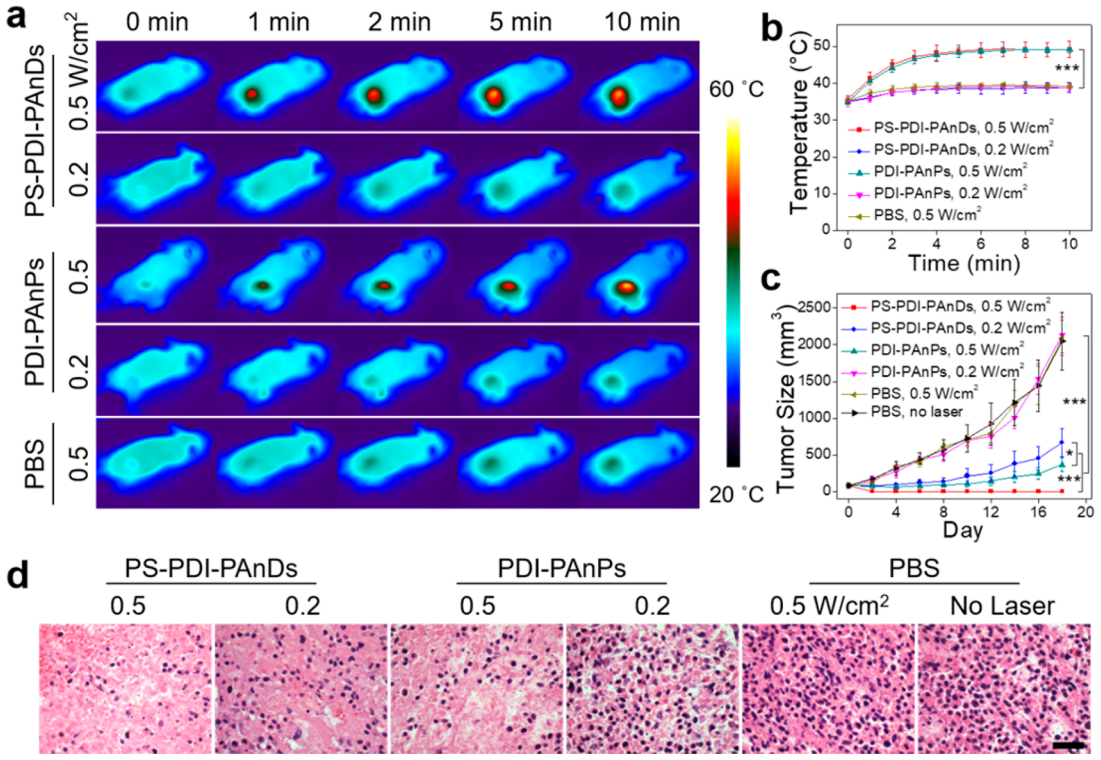

Figure 5. Combinational PTT/Oxy-PDT treatment studies with the PS-PDI-PAnDs. (a) Thermographic images of mice treated with a photoirradiation (671 nm, 0.5 W/cm^2 or 0.2 W/cm^2, 10 min) at 24 h p.i. of nanotherapeutic agents. (b) Temperature curves at tumor regions based on (a). Only tumors treated with a 0.5 W/cm^2 irradiation plus PS-PDI-PAnDs or PDI-PAnPs injection induced significant temperature increase. The tumor temperature raised rapidly and maintained at 49 °C. In contrast, a 0.2 W/cm^2 irradiation plus PS-PDI-PAnDs or PDI-PAnPs injection could only heated the tumors to about 39 °C. And a 0.5 W/cm^2 irradiation plus PBS injection heated the tumors to around 39 °C as well. (c) Tumor growth curves. Complete tumor eradication was found in the combinational PTT/Oxy-PDT treatment group with i.v. injection of PS-PDI-PAnDs plus a 0.5 W/cm^2 laser irradiation. Significant tumor growth inhibition was also observed with animals treated with PTT only (i.v. injection of PS-PDI-PAnPs plus a 0.5 W/cm^2 laser irradiation) and Oxy-PDT only (i.v. injection of PS-PDI-PAnDs plus a 0.2 W/cm^2 laser irradiation), indicating TGI rates of 82.3% and 67.5%, respectively, on day 18. (d) H&E staining of tumors acquired at 24-h after therapy. The tumors from the combinational PTT/Oxy-PDT, PTT only, and Oxy-PDT only treatment groups showed extensive cell death and severe structure destruction. The treatment efficacy was much significant in the combinational PTT/Oxy-PDT group. Scale bar, 100 μm. *P < 0.05. ***P < 0.001.

tumors but negligible fluorescence in the PS-PDI-PAnD-treated ones. All these results demonstrated enhanced tumor oxygen level in Oxy-PDT comparted to conventional PDT. According to these observations, an irradiation fluence of 0.2 W/cm^2 and irradiation time of 10 min were chosen for the Oxy-PDT in the subsequent therapy studies. Further increasing the irradiation fluence did not benefit to the Oxy-PDT efficacy.

Combinational PTT/Oxy-PDT Treatment. Despite effective tumor damage from Oxy-PDT, combination of PTT and PDT have reported to induce synergistic treatment efficacies and offer unique advantages over PDT alone.[38] In the case of PS-PDI-PAnDs, both PTT and Oxy-PDT effect were activated by laser at wavelength of 671 nm. Therefore, a simultaneous PTT and Oxy-PDT could be achieved with the PS-PDI-PAnDs upon a single laser irradiation, which could avoid a time interval between PTT and PDT, thus leading to optimal synergistic therapeutic efficacy.[38] Encouraging by the efficient *in vitro* photothermal conversion (Figure 1e and 1f), we evaluated the *in vivo* PTT effect with the PS-PDI-PAnDs on U87MG tumor model. Moderate *in vivo* photothermal conversion efficiency was observed in Figure S15 at irradiation fluences of 0.3 W/cm^2 and below (671 nm, 10 min). However, when the irradiation fluence was raised to 0.5 W/cm^2, the PS-PDI-PAnDs efficiently heated the tumors and maintained the temperature at around 49 °C for PTT treatment (Figure 5a and 5b). In contrast, there was little temperature changes for tumors irradiated with a 0.5 W/cm^2 laser and treated with PBS. Therefore, although triggered by the same 671 nm laser, we could easily differentiate the efficacy from PTT and Oxy-PDT by controlling the irradiation fluence. A 0.5 W/cm^2 irradiation was used for PTT only or combinational PTT/Oxy-PDT treatment, while a 0.2 W/cm^2 irradiation was applied for Oxy-PDT only treatment.

Combinational PTT/Oxy-PDT therapy studies were carried out on the same U87MG tumor model (n = 5). Specifically, the PS-PDI-PAnDs were administrated into the mice at a dosage of 200 μL of 5 mg PDI/mL. After 24 h, we irradiated the tumors with a 671 nm laser at 0.5 W/cm^2 for 10 min. For PTT treatment only group, the mice were treated with PDI-PAnPs (without PFC and PSs loading) and received the same 0.5 W/cm^2 irradiation. For Oxy-PDT treatment only group, we i.v. injected the mice with PS-PDI-PAnDs, but irradiated the tumors with a lower irradiation fluence at 0.2 W/cm^2. An injection of PDI-PAnPs followed by a 0.2 W/cm^2 photoirradiation was also performed as control. All nanotheranostic agents were injected at the same PDI dosage and the tumors were irradiated with a 671 nm laser for 10 min at 24-h p.i. For further controls, animals were injected with PBS and received with or without photoirradiation in separate groups.

DOI: 10.1021/acsnano.7b08628
ACS Nano 2018, 12, 2610−2622

The combinational PTT/Oxy-PDT treatment induced significant tumor inhibition, showing 100% tumor eradication after the photoirradiation. Both the PTT only and the Oxy-PDT only groups demonstrated significant tumor growth inhibition. Comparing to the PBS control group, tumor growth inhibition (TGI) rates of 82.3 ± 6.4% and 67.5 ± 9.1% were observed on day 18, respectively (Figure 5c). In contrast, the PDI-PAnPs plus a 0.2 W/cm^2 photoirradiation showed minimal tumor inhibition, suggesting the PDI components made negligible contributions in the treatment efficacy of the Oxy-PDT only group. After the therapy, tumors and major organs were acquired for histological analysis. H&E staining on the tumor sections 24-h post irradiation found extensive cell killing and tumor structure disruption in the treatment group comparing to the controls (Figure 5d). Despite the efficient tumor killing, no significant mice body weight drop was observed during the treatment (Figure S17). In addition, no pathological abnormalities were found in major organs from H&E staining (Figure S18), indicating minimal side effects in the treatment. To further confirm the oxygen contribution during the combinational therapy, another two controls were studied by i.v. injecting U87MG tumor-bearing mice with the PS-PDI-PAnPs, followed by a 0.5 or 0.2 W/cm^2 laser irradiation. Thermal images of the irradiated tumors were recorded and quantified (Figure S19). Potential photothermal killing could only occurred in tumors irradiated at 0.5 W/cm^2 but not at 0.2 W/cm^2. The combinational PDT/PTT and conventional PDT showed a TGI of 92.1 ± 4.8% and 62.5 ± 11.4 on day 18, respectively, which was significantly lower than the corresponding Oxy-PDT involved treatment (Figure S20). These results again validated that the PFC, or the sufficient and sustained O_2 release from the PFC, remarkably contributed to the Oxy-PDT efficacy. In addition, severe tumor architecture disruption was found in the combinational PDT/PTT-treated tumors (Figure S20c). Minimal side effects were induced by the PS-PDI-PAnPs plus irradiation treatment, since no obvious mice body weight drop (Figure S21a) and no pathological abnormalities in major organs (Figure S21b) were observed.

The effective tumor eradication of the combinational PTT/Oxy-PDT may result from several synergistic effects. First, at the beginning of the irradiation, a mild hyperthermia may increase the blood flow and broaden the endothelial gaps in tumors, thus improving the delivery of PS-PDI-PAnDs and oxygen.[38] A mild hyperthermia could also increase the permeability of cell membranes to boost the intracellular concentration of the PS-PDI-PAnDs, leading to enhanced intracellular $^1O_2$ concentration for promoted PDT efficacy.[38] Second, as the irradiation went on, the vasculatures surrounded by the PS-PDI-PAnDs would be destroyed, enabling further tumor penetration of the nanotherapeutic agents.[48] Third, as continuously irradiated, more nanodroplets were vaporized at the tumor sites, resulting in a cavitation effect for induction of strong biological and physiochemical functions in tumors,[42] such as enhanced cell membrane permeability, enlarged endothelial gaps, damaged microvessels, and disturbed tumor structures,[6] therefore achieving deeper penetration of the PS-PDI-PAnDs as well as its constituents. Fourth, the laser irradiation may result in a burst release of O_2 from the PS-PDI-PAnDs, resulting in instant oxygenation of the whole tumors and markedly enhanced PDT efficacy.[41] Furthermore, both the PTT and PDT could activate immune responses for further cancer killing.[38,49] Taken together, all these effects led to a complete tumor eradication in the combinational PTT/Oxy-PDT with the PS-PDI-PAnDs. Future studies will be needed to illustrate the full mechanisms behind the effective tumor suppression.

CONCLUSIONS

In summary, a type of PFC nanodroplets that cointegrated with photoabsorbers and photosensitizers were successfully developed. This biocompatible PS-PDI-PAnDs have been demonstrated to be excellent PA and US contrast agents. Their nanoscale size rendered them high tumor accumulation *via* the EPR effect. Upon a single 671 nm laser irradiation, on the one hand, the PDI stabilizing shell can efficiently convert light energy into heat, initiate the vaporization of the liquid PFC for US imaging, as well as kill cancerous cells *via* photothermal effect. On the other hand, the encapsulated PSs can transfer light energy to the nearby O_2, by taking advantages of the sufficient and sustained O_2 supply from the oxygen-self-enriched PFC, and produce a significantly higher amount of cytotoxic $^1O_2$ than conventional PDT, therefore achieving a promoted photodynamic killing effect. We expect that this PS-PDI-PAnD formulation finds great potential in clinical translations in dual-modal PA/US imaging-guided combinational cancer therapy.

METHODS

Preparation of PS-PDI-PAnDs, PS-PDI-PAnPs, and PDI-PAnPs. To prepare PS-PDI-PAnDs, PEG-based PDI (Structure 1, Figure S1) and amine functional PEG-based PDI (Structure 2, Figure S1) molecules were first synthesized by following our previous publication.[31] The two PDI molecules were dissolved in 2 mL of precooled tetrahydrofuran (THF) at a molar ratio of 9:1. Then, $ZnF_{16}Pc$/THF solution and 100 μL of precooled perfluoropentane were added. The mixture was briefly sonicated and dropwise added with 1 mL of water under rapid stirring. Next, THF was removed by an argon flow on the solution surface under stirring at room temperature. Unloaded $ZnF_{16}Pc$ molecules were removed by precipitation in aqueous solution due to their high hydrophobicity. The resulting PS-PDI-PAnDs in the supernatant were reconstituted in PBS and filtered through a 0.22 μm filter for the following cell and animal experiments. The $ZnF_{16}Pc$ encapsulation efficiency was assessed spectroscopically by comparing the unloaded $ZnF_{16}Pc$ molecules to a predetermined standard curve. A formulation of the final PS-PDI-PAnDs with a PDI to $ZnF_{16}Pc$ molar ratio of around 10:1 was used for further studies. For dye labeling, PS-PDI-PAnDs were incubated with IRDye800-NHS (LI-COR) at an initial molar ratio of 5:1 for 30 min and then purified through a NAP-5 column to remove the uncoupled dye molecules. For *in vitro* and *in vivo* Oxy-PDT, the PS-PDI-PAnDs were presaturated with O_2 by soaking in an industrial grade O_2 for 15 min at a flow rate of 5 mL/h.[44,50] PS-PDI-PAnPs and PDI-PAnPs were also prepared as controls based on our previous publication.[31] To prepare PS-PDI-PAnPs, the two PDI molecules (at a molar ratio of 9:1) and $ZnF_{16}Pc$ molecules were dissolved in 2 mL tetrahydrofuran (THF). Next, 1 mL of H_2O was slowly dropped into the solution with rapid stirring. Then, THF was removed by an argon flow on the solution surface under stirring at room temperature. The initial concentration of PDI and $ZnF_{16}Pc$ was carefully tuned to achieve the final molar ratio of 10:1 in the resulting PS-PDI-PAnPs. To prepare PDI-PAnPs, a starting THF solution consisting of the PDI molecules only was used. TEM images were acquired on a Jeol JEM 2010 electron microscope at an acceleration voltage of 200 kV. DLS data was recorded on a Malvern ZetaSizer Nano instrument. UV−vis absorption spectra were recorded by using a Shimadzu UV-2501 spectrophotometer.

Photothermal Heating. Both an irradiation fluence-dependent and a PDI concentration-dependent photothermal effect were carefully assessed. To evaluate the irradiation fluence-dependent photothermal effect, PS-PDI-PAnD solutions at a concentration of 0.1 mg PDI/mL

DOI: 10.1021/acsnano.7b08628
ACS Nano 2018, 12, 2610−2622

were irradiated with a 671 nm laser at different irradiation fluence (0.1, 0.3, 0.5, 0.8, 1, 1.2 W/cm^2) for 5 min. To evaluate the PDI concentration-dependent photothermal effect, PS-PDI-PAnD solutions at different concentrations (0.1, 0.2, 0.5, 1 mg PDI/mL) were irradiated with a 671 nm laser at 0.5 W/cm^2 for 5 min. A distilled water sample irradiated with a 671 nm laser at 1.2 W/cm^2 for 5 min was used as a control. A SC300 infrared camera was used to record thermal images and quantify the temperature of the solutions during the irradiation.

***In Vitro* PA and US Imaging.** PS-PDI-PAnD solutions at different concentrations (0, 0.0625, 0.125, 0.25, 0.5, 1 mg PDI/mL) were filled into polyethylene 50 capillaries. The capillaries were positioned in a water bath and imaged from the top using a 40 MHz, 256-element linear array transducer with a Visual Sonic Vevo 2100 LAZR system. The PA signals were quantified as the average pixel intensities from the region of interests (ROIs). For US imaging, a 671 nm laser beam was used to irradiate the sample from the side. The US signals were collected and compared before and after the irradiation. To investigate the ODV event, PS-PDI-PAnD solutions were filled in either a sealed slide or a cap-open PE tube. Photographs were taken before and after the laser irradiation (671 nm, 0.5 W/cm^2, 3 min) in both situations. The solutions after irradiation were also subjected to TEM analysis.

Cell Line and Animal Models. The U87MG human glioblastoma cell line was obtained from the American Type Culture Collection and cultured with Dulbecco's Modified Eagle Medium (DMEM) in a cell culture flask. The HUVEC human endothelial cell line and NIH/3T3 mouse embryo fibroblast cell line were cultured with Endothelial Cell Growth Kit-VEGF medium and DMEM, respectively. Athymic nude mice and balb/c mice were purchased from Envigo laboratories. The tumor model was established by subcutaneously injection of around 5 × 10^6 U87MG cells into the mice right hind limb. All the experimental procedures had been conducted following a protocol approved by the animal care and use committee (ACUC) of the National Institutes of Health Clinical Center (NIHCC).

MTT Assay. Around 1 × 10^4 U87MG cells were seeded in each well of a 96-well plate and incubated overnight. PS-PDI-PAnDs with different PDI concentrations (0, 10, 50, 100, 200, and 400 μg/mL) were then added to the plate. For comparison, PS-PDI-PAnPs and PDI-PAnPs at the same PDI concentration gradients were also studied. After a 24-h incubation, a laser irradiation at 0.1 W/cm^2 was applied to each well for 200 s. Subsequently, the medium of each well was removed; the U87MG cells were washed twice with PBS and replenished with fresh medium. After incubating for another 24 h, MTT assay was performed to determine the cell viability. For controls, no irradiation was applied. In addition, MTT assays were conducted on HUVEC and NIH/3T3 cells to evaluate the biocompatibility of the PS-PDI-PAnDs. To investigate the impact of oxygen release rate on the PDT efficiency, U87MG cells were incubated in a humidified hypoxic environment (1% O_2/5% CO_2/94% N_2) at 37 °C. After overnight incubation with PS-PDI-PAnDs, the cells irradiated with a 671 nm laser at 0.1 W/cm^2 for 200 s at room temperature or 42 °C in separate groups. In a control group, cells were treated with PS-PDI-PAnPs and received the irradiation at room temperature. MTT assay was then conducted to measure the cell viability.

Live and Dead Assay. A live/dead cell double staining kit (Sigma, 04511) was used to assess phototoxicity. Approximately 1 × 10^5 U87MG cells were seeded in each well of a 4-well cell culture chamber for an overnight incubation. Then, PS-PDI-PAnDs or PS-PDI-PAnPs (at the same concentration of 100 μg PDI/mL) was added and incubated with the U87MG cells for another 24 h. A laser irradiation (671 nm, 0.1 W/cm^2, 200 s) was applied 24 h before the addition of the Calcium AM/PI working solution. After a 30 min incubation, the cell culture medium was removed and the cells were washed with PBS. The slides were mounted and were then observed under a fluorescence microscope.

$^1O_2$ Production. A singlet oxygen sensor green reagent (SOSG, S36002, Invitrogen) was used as a $^1O_2$ indicator. A solution containing PS-PDI-PAnDs and SOSG reagent was added into a cap-open cuvette. The cuvette was irradiated with a 671 nm laser (0.1 W/cm^2) and kept in the dark. At selected time points (1, 2, 4, 6, 8, 10 min), the amount of $^1O_2$ in the solution was determined by measuring fluorescence intensities at 525 nm. In the control group, PS-PDI-PAnPs at the same photosensitizer concentrations were tested. In addition, to test the $^1O_2$ generation performance under a low oxygen conditions, the experiment was repeated in a sealed cuvette that was deoxidized by pumping with ultrahigh pure argon gas. For cell studies, U87MG cells were seeded in a 4-well cell culture chamber and were incubated overnight. Next, PS-PDI-PAnDs or PS-PDI-PAnPs (at the same PDI concentration of 100 μg/mL) were added and incubated with the U87MG cells for another 24 h. Then, 1 μL of SOSG working solution was added to the U87MG cells 30 min prior to the laser irradiation (671 nm, 0.1 W/cm^2, 200 s). Subsequently, the incubation medium was removed and the U87MG cells were washed with PBS. The slides were mounted with mounting medium with DAPI (*VECTASHIELD*, Catalog Number: H-1200) and were observed under a Zeiss LSM 780 confocal microscope.

Oxygen Release Measurements. The oxygen concentrations in aqueous solution were recorded in real time by a portable pinpoint dissolved oxygen meter (PENTAIR, Catalog #: DO62) in a sealed and N_2-filled 50 mL centrifuge tube. To explore the oxygen release at different temperatures, deoxygenated water (N_2 pretreated) was first injected into the tube and followed by an addition of the oxygen-saturated PS-PDI-PAnDs. After 5 min, the tube was put into a 42 °C water bath for 5 min and then put back to room temperature. A total of 15 min was recorded for the oxygen concentration. As a control, oxygen concentration in deoxygenated water was measured.

***In Vitro* Cellular Hypoxia Detection.** Approximately 1 × 10^5 U87MG cells were seeded in each well of a 4-well cell culture chamber and were incubated overnight in a low-oxygen atmosphere (1% O_2/5% CO_2/94% N_2) at 37 °C. The hypoxic U87MG cells were then incubated overnight with oxygen-saturated PS-PDI-PAnDs. The intracellular oxygen level was detected by an oxygen indicator $[Ru(dpp)_3]Cl_2$. In a separate group, hypoxic U87MG cells were incubated with the PS-PDI-PAnDs overnight, following by a 200 s of incubation at 42 °C. For controls, the hypoxic cells were treated with PS-PDI-PAnPs or PBS.

***In Vivo* Blood Circulation Half-Lives and Tissue Distribution.** The PS-PDI-PAnDs (200 μL of 5 mg PDI/mL) were intravenously injected into healthy bab/c mice (n = 3). At 2 min, 5 min, 10 min, 30 min, 1, 2, 4, 8, 24, and 48 h p.i., 20 μL of blood was collected and mixed with 10 μL of 10 mM EDTA solution. The PDI concentration in plasma was measured by comparing its absorbance spectrum to a predetermined standard curve. The blood circulation half-life curve was fitted with a single-compartment pharmacokinetic model. At 48 h p.i., major organs (*i.e.*, heart, liver, spleen, lung, kidney) were acquired, washed with PBS, excised, and homogenized. The homogenized mixture was centrifuged and the supernatant was collected for the measurement of the PDI concentration.

***In Vivo* Tumor Optical, PA and US Imaging.** The imaging studies started when tumors reached a size between 200 and 500 mm^3. For *in vivo* near-infrared fluorescent imaging, IRDye800 labeled PS-PDI-PAnDs (200 μL of 5 mg PDI/mL) were intravenously injected into U87MG-bearing mice (n = 3). Images were taken on a Maestro II imaging system (PerkinElmer Inc.) at 1, 2, 4, 24, and 48 h post injection (p.i.) time points. ROIs were circled around the tumors, and the optical intensities in total scaled counts per second were read by the Maestro software. After the 48-h imaging, tumors and major organs were collected for *ex vivo* imaging. The images were analyzed with the Maestro software. For *in vivo* tumor PA imaging, the PS-PDI-PAnDs (200 μL of 5 mg PDI/mL) were intravenously injected into U87MG-bearing mice and the tumors was imaged with an Endra Nexus 128 PA tomography system (Endra, Inc., Ann Arbor, MI. Seven ns pulses, 20 Hz pulse repetition frequency, wavelength ranges of 680−950 nm, 7 mJ/pulse on the animal surface). PA images were acquired and quantified at different time points. At 48 h p.i., tumors and major organs were collected for *ex vivo* imaging with a Visual Sonic Vevo 2100 LAZR system. For *in vivo* US imaging, U87MG-bearing mice were administrated with the PS-PDI-PAnDs (200 μL of 5 mg PDI/mL). At 24-h p.i., a laser irradiation (0.5 W/cm^2, 3 min) was applied. US signals were collected under B-mode before and after the

DOI: 10.1021/acsnano.7b08628
ACS Nano 2018, 12, 2610−2622

irradiation by using a Visual Sonic Vevo 2100 LAZR system equipped with a 40 MHz, 256-element linear array transducer. For controls, the PS-PDI-PAnPs at the same PDI concentrations were intravenously injected into U87MG tumor bearing mice for the PA and US imaging studies. To investigate the changes of tumor oxygenation during the PDT treatment, PA images of oxygenated hemoglobin (λ = 850 nm) at tumors were recorded and quantified before and after 24 h of the intravenously injection of the PS-PDI-PAnDs. Then, a 671 nm laser at 0.2 W/cm^2 was irradiated at the tumor areas. After 30 min of the irradiation, PA images (λ = 850 nm) of the tumors were acquired and measured. The PS-PDI-PAnPs treated tumors were also imaged as a control.

Fluence-Dependent *In Vivo* Oxy-PDT. PS-PDI-PAnDs and PS-PDI-PAnPs (200 μL of 5 mg PDI/mL) were intravenously injected into U87MG bearing mice in separate groups. After 24 h, the tumors were irradiated by a 671 nm laser at different fluence rates (0.3, 0.25, 0.2, 0.1 W/cm^2) for 10 min. Real-time thermal images of the mice were recorded with a SC300 infrared camera during the irradiation. 24 h after the irradiation, the tumors were acquired and were subjected to hematoxylin and eosin (H&E) staining and TUNEL assay.

TUNEL Assay and HIF-1α Staining. TUNEL assay for cryogenic sections were performed according to a protocol provided by the vendor (Roche, Catalog #: 6432344001). 15 μm of slides were prepared and fixed with 4% paraformaldehyde in PBS (pH 7.4) for 10 min at room temperature. After washing with PBS, the slides were incubated in permeabilization solution (0.1% Triton X-100, 0.1% sodium citrate in water, freshly prepared) on ice for 2 min. After another washing cycle, the tumor samples were incubated with TUNEL reaction mixture in the dark for 60 min at 37 °C in a humidified atmosphere. After gently rising with PBS, the slides were mounted with mounting medium with DAPI (*VECTASHIELD*, Catalog #: H-1200) and ready for confocal microscopic imaging. For HIF-1α staining, the paraformaldehyde fixed slides were permeabilized with 0.1% Triton X-100 in a 0.1% sodium citrate aqueous solution and blocked with 2% BSA/PBS for 30 min at room temperature. The slides were then stained with a HIF-1 alpha monoclonal antibody (Invitrogen, Catalog #: MA1−516) at a dilution of 1:100 overnight at 4 °C. After washing with PBS, the slides were labeled with an Alexa Fluor 488-conjugated goat antimouse IgG (H+L) secondary antibody (Invitrogen, Catalog #: A28175) at a dilution of 1:500 for 45 min at room temperature and mounted with mounting medium with DAPI (*VECTASHIELD*, Catalog #: H-1200).

Combinational PTT/Oxy-PDT Therapy Studies. The therapy studies were performed on U87MG tumor models. Thirty 5- to 6-week-old female nude mice were subcutaneously injected with 3 × 10^6 U87-MG cells on the right hind limbs. The 30 mice were randomly divided into 6 groups, 5 mice per group. The study started when the tumor size reached around 100 mm^3. For the treatment group, the mice were first intravenously injected with PS-PDI-PAnDs (200 μL of 5 mg PDI/mL). After 24 h, the tumors were irradiated by a 671 nm laser at 0.5 W/cm^2 for 10 min. The five control groups received: (1) PDI-PAnPs and irradiation (0.5 W/cm^2, 10 min); (2) PS-PDI-PAnDs and irradiation (0.2 W/cm^2, 10 min); (3) PDI-PAnPs and irradiation (0.2 W/cm^2, 10 min); (4) PBS and irradiation (0.5 W/cm^2, 10 min); and (5) PBS only. To investigate the contribution of PFC to the Oxy-PDT, another two control groups (n = 5) with PS-PDI-PAnPs injection plus irradiation (671 nm, 0.5 or 0.2 W/cm^2, 10 min) were studied and compared to that with the PS-PDI-PAnDs injection and the same irradiation, respectively. All groups of mice were injected with the same dosage of PDI and irradiated 24 h after the injections. Real-time thermal images of the mice were recorded with a SC300 infrared camera during the irradiation. During the therapy, the tumor sizes and body weights were measured every other day. Tumor sizes were measured and calculated by following the formula: size (mm^3) = length (mm) × width (mm)^2/2. After therapy, the major organs were collected and subjected to paraffin-embedded H&E staining. To better evaluate the treatment efficacy, in a separate study, tumors were collected at 24-h postirradiation and subjected to paraffin-embedded H&E staining.

Statistical Methods. Quantitative data were expressed as mean ± SD. Means were compared using Student's t test. $P < 0.05$ was considered statistically significant.

ASSOCIATED CONTENT

Supporting Information

The Supporting Information is available free of charge on the ACS Publications website at DOI: 10.1021/acsnano.7b08628.

Additional experimental data (Figures S1−S21) (PDF)

AUTHOR INFORMATION

Corresponding Authors

*E-mail: zhen.yang3@nih.gov.
*E-mail: iamqlfan@njupt.edu.cn.
*E-mail: shawn.chen@nih.gov.

ORCID

Zhen Yang: 0000-0003-4056-0347
Jibin Song: 0000-0003-4771-5006
Yunlu Dai: 0000-0003-4023-7320
Quli Fan: 0000-0002-9387-0165
Xiaoyuan Chen: 0000-0002-9622-0870

Notes

The authors declare no competing financial interest.

ACKNOWLEDGMENTS

This work was supported by intramural research program of the National Institute of Biomedical Imaging and Bioengineering (NIBIB), National Institutes of Health (NIH).

REFERENCES

(1) Huang, Y.; Vezeridis, A. M.; Wang, J.; Wang, Z.; Thompson, M.; Mattrey, R. F.; Gianneschi, N. C. Polymer-Stabilized Perfluorobutane Nanodroplets for Ultrasound Imaging Agents. *J. Am. Chem. Soc.* **2017**, *139*, 15−18.

(2) Klibanov, A. L. Targeted Delivery of Gas-Filled Microspheres, Contrast Agents for Ultrasound Imaging. *Adv. Drug Delivery Rev.* **1999**, *37*, 139−157.

(3) Yoon, Y. I.; Tang, W.; Chen, X. Ultrasound-Mediated Diagnosis and Therapy Based on Ultrasound Contrast Agents. *Small Methods* **2017**, *1*, 1700173−1700185.

(4) Wilson, K.; Homan, K.; Emelianov, S. Biomedical Photoacoustics Beyond Thermal Expansion Using Triggered Nanodroplet Vaporization for Contrast-Enhanced Imaging. *Nat. Commun.* **2012**, *3*, 618−627.

(5) Santiesteban, D. Y.; Dumani, D. S.; Profili, D.; Emelianov, S. Y. Copper Sulfide Perfluorocarbon Nanodroplets as Clinically Relevant Photoacoustic/Ultrasound Imaging Agents. *Nano Lett.* **2017**, *17*, 5984−5989.

(6) Tang, H.; Zheng, Y.; Chen, Y. Materials Chemistry of Nanoultrasonic Biomedicine. *Adv. Mater.* **2017**, *29*, 201604105−201604126.

(7) Song, X.; Feng, L.; Liang, C.; Yang, K.; Liu, Z. Ultrasound Triggered Tumor Oxygenation with Oxygen-Shuttle Nanoperfluorocarbon to Overcome Hypoxia-Associated Resistance in Cancer Therapies. *Nano Lett.* **2016**, *16*, 6145−6153.

(8) Fan, X.; Wang, L.; Guo, Y.; Xiong, X.; Zhu, L.; Fang, K. Inhibition of Prostate Cancer Growth Using Doxorubicin Assisted by Ultrasound-Targeted Nanobubble Destruction. *Int. J. Nanomed.* **2016**, *11*, 3585−3596.

(9) Fan, X.; Wang, L.; Guo, Y.; Tu, Z.; Li, L.; Tong, H.; Xu, Y.; Li, R.; Fang, K. Ultrasonic Nanobubbles Carrying Anti-PSMA Nanobody: Construction and Application in Prostate Cancer-Targeted Imaging. *PLoS One* **2015**, *10*, e0127419−e0127431.

DOI: 10.1021/acsnano.7b08628
ACS Nano 2018, 12, 2610−2622

(10) Fan, X.; Guo, Y.; Wang, L.; Xiong, X.; Zhu, L.; Fang, K. Diagnosis of Prostate Cancer Using Anti-PSMA Aptamer A10−3.2-Oriented Lipid Nanobubbles. *Int. J. Nanomed.* **2016**, *11*, 3939−3950.
(11) Huang, H. Y.; Hu, S. H.; Hung, S. Y.; Chiang, C. S.; Liu, H. L.; Chiu, T. L.; Lai, H. Y.; Chen, Y. Y.; Chen, S. Y. SPIO Nanoparticle-Stabilized PAA-F127 Thermosensitive Nanobubbles with MR/US Dual-Modality Imaging and HIFU-Triggered Drug Release for Magnetically Guided In Vivo Tumor Therapy. *J. Controlled Release* **2013**, *172*, 118−127.
(12) Lin, P. L.; Eckersley, R. J.; Hall, E. A. H. Ultrabubble: A Laminated Ultrasound Contrast Agent with Narrow Size Range. *Adv. Mater.* **2009**, *21*, 3949−3952.
(13) Huang, H. Y.; Liu, H. L.; Hsu, P. H.; Chiang, C. S.; Tsai, C. H.; Chi, H. S.; Chen, S. Y.; Chen, Y. Y. A Multitheragnostic Nanobubble System to Induce Blood-Brain Barrier Disruption with Magnetically Guided Focused Ultrasound. *Adv. Mater.* **2015**, *27*, 655−661.
(14) Paproski, R. J.; Forbrich, A.; Huynh, E.; Chen, J.; Lewis, J. D.; Zheng, G.; Zemp, R. J. Porphyrin Nanodroplets: Sub-micrometer Ultrasound and Photoacoustic Contrast Imaging Agents. *Small* **2016**, *12*, 371−380.
(15) Sheeran, P. S.; Luois, S.; Dayton, P. A.; Matsunaga, T. O. Formulation and Acoustic Studies of a New Phase-Shift Agent for Diagnostic and Therapeutic Ultrasound. *Langmuir* **2011**, *27*, 10412−10420.
(16) Ho, Y. J.; Yeh, C. K. Theranostic Performance of Acoustic Nanodroplet Vaporization-Generated Bubbles in Tumor Intertissue. *Theranostics* **2017**, *7*, 1477−1488.
(17) Hannah, A.; Luke, G.; Wilson, K.; Homan, K.; Emelianov, S. Indocyanine Green-Loaded Photoacoustic Nanodroplets: Dual Contrast Nanoconstructs for Enhanced Photoacoustic and Ultrasound Imaging. *ACS Nano* **2014**, *8*, 250−259.
(18) Hannah, A. S.; VanderLaan, D.; Chen, Y. S.; Emelianov, S. Y. Photoacoustic and Ultrasound Imaging Using Dual Contrast Perfluorocarbon Nanodroplets Triggered by Laser Pulses at 1064 nm. *Biomed. Opt. Express* **2014**, *5*, 3042−3052.
(19) Strohm, E.; Rui, M.; Gorelikov, I.; Matsuura, N.; Kolios, M. Vaporization of Perfluorocarbon Droplets Using Optical Irradiation. *Biomed. Opt. Express* **2011**, *2*, 1432−1442.
(20) Sharifi, S.; Behzadi, S.; Laurent, S.; Forrest, M. L.; Stroeve, P.; Mahmoudi, M. Toxicity of Nanomaterials. *Chem. Soc. Rev.* **2012**, *41*, 2323−2343.
(21) Balasubramanian, S. K.; Jittiwat, J.; Manikandan, J.; Ong, C. N.; Yu, L. E.; Ong, W. Y. Biodistribution of Gold Nanoparticles and Gene Expression Changes in the Liver and Spleen after Intravenous Administration in Rats. *Biomaterials* **2010**, *31*, 2034−2042.
(22) Ungureanu, C.; Kroes, R.; Petersen, W.; Groothuis, T. A.; Ungureanu, F.; Janssen, H.; van Leeuwen, F. W.; Kooyman, R. P.; Manohar, S.; van Leeuwen, T. G. Light Interactions with Gold Nanorods and Cells: Implications for Photothermal Nanotherapeutics. *Nano Lett.* **2011**, *11*, 1887−1894.
(23) Pu, K.; Shuhendler, A. J.; Jokerst, J. V.; Mei, J.; Gambhir, S. S.; Bao, Z.; Rao, J. Semiconducting Polymer Nanoparticles as Photoacoustic Molecular Imaging Probes in Living Mice. *Nat. Nanotechnol.* **2014**, *9*, 233−239.
(24) Pu, K.; Mei, J.; Jokerst, J. V.; Hong, G.; Antaris, A. L.; Chattopadhyay, N.; Shuhendler, A. J.; Kurosawa, T.; Zhou, Y.; Gambhir, S. S.; Bao, Z.; Rao, J. Diketopyrrolopyrrole-Based Semiconducting Polymer Nanoparticles for In Vivo Photoacoustic Imaging. *Adv. Mater.* **2015**, *27*, 5184−5190.
(25) Miao, Q.; Lyu, Y.; Ding, D.; Pu, K. Semiconducting Oligomer Nanoparticles as an Activatable Photoacoustic Probe with Amplified Brightness for In Vivo Imaging of pH. *Adv. Mater.* **2016**, *28*, 3662−3668.
(26) Lyu, Y.; Zhen, X.; Miao, Y.; Pu, K. Reaction-Based Semiconducting Polymer Nanoprobes for Photoacoustic Imaging of Protein Sulfenic Acids. *ACS Nano* **2017**, *11*, 358−367.
(27) Xie, C.; Zhen, X.; Lyu, Y.; Pu, K. Nanoparticle Regrowth Enhances Photoacoustic Signals of Semiconducting Macromolecular Probe for In Vivo Imaging. *Adv. Mater.* **2017**, *29*, 201703693−201703699.
(28) Yin, C.; Zhen, X.; Fan, Q.; Huang, W.; Pu, K. Degradable Semiconducting Oligomer Amphiphile for Ratiometric Photoacoustic Imaging of Hypochlorite. *ACS Nano* **2017**, *11*, 4174−4182.
(29) Fan, Q.; Cheng, K.; Yang, Z.; Zhang, R.; Yang, M.; Hu, X.; Ma, X.; Bu, L.; Lu, X.; Xiong, X.; Huang, W.; Zhao, H.; Cheng, Z. Perylene-Diimide-Based Nanoparticles as Highly Efficient Photoacoustic Agents for Deep Brain Tumor Imaging in Living Mice. *Adv. Mater.* **2015**, *27*, 843−847.
(30) Yang, Z.; Song, J.; Dai, Y.; Chen, J.; Wang, F.; Lin, L.; Liu, Y.; Zhang, F.; Yu, G.; Zhou, Z.; Fan, W.; Huang, W.; Fan, Q.; Chen, X. Self-Assembly of Semiconducting-Plasmonic Gold Nanoparticles with Enhanced Optical Property for Photoacoustic Imaging and Photothermal Therapy. *Theranostics* **2017**, *7*, 2177−2185.
(31) Yang, Z.; Tian, R.; Wu, J.; Fan, Q.; Yung, B. C.; Niu, G.; Jacobson, O.; Wang, Z.; Liu, G.; Yu, G.; Huang, W.; Song, J.; Chen, X. Impact of Semiconducting Perylene Diimide Nanoparticle Size on Lymph Node Mapping and Cancer Imaging. *ACS Nano* **2017**, *11*, 4247−4255.
(32) Cheng, Y.; Cheng, H.; Jiang, C.; Qiu, X.; Wang, K.; Huan, W.; Yuan, A.; Wu, J.; Hu, Y. Perfluorocarbon Nanoparticles Enhance Reactive Oxygen Levels and Tumour Growth Inhibition in Photodynamic Therapy. *Nat. Commun.* **2015**, *6*, 8785−8792.
(33) Gao, M.; Liang, C.; Song, X.; Chen, Q.; Jin, Q.; Wang, C.; Liu, Z. Erythrocyte-Membrane-Enveloped Perfluorocarbon as Nanoscale Artificial Red Blood Cells to Relieve Tumor Hypoxia and Enhance Cancer Radiotherapy. *Adv. Mater.* **2017**, *29*, 201701429−201701435.
(34) Song, G.; Ji, C.; Liang, C.; Song, X.; Yi, X.; Dong, Z.; Yang, K.; Liu, Z. TaOx Decorated Perfluorocarbon Nanodroplets as Oxygen Reservoirs to Overcome Tumor Hypoxia and Enhance Cancer Radiotherapy. *Biomaterials* **2017**, *112*, 257−263.
(35) Riess, J. G. Oxygen Carriers ("Blood Substitutes")—Raison d'Etre, Chemistry, and Some Physiology. *Chem. Rev.* **2001**, *101*, 2797−2920.
(36) Castro, C. I.; Briceno, J. C. Perfluorocarbon-Based Oxygen Carriers: Review of Products and Trials. *Artif. Organs* **2010**, *34*, 622−634.
(37) Fuhrman, B. P.; Paczan, P. R.; DeFrancisis, M. Perfluorocarbon-Associated Gas Exchange. *Crit. Care Med.* **1991**, *19*, 712−722.
(38) Fan, W.; Yung, B.; Huang, P.; Chen, X. Nanotechnology for Multimodal Synergistic Cancer Therapy. *Chem. Rev.* **2017**, *117*, 13566−13638.
(39) Garcia, A. M.; Alarcon, E.; Munoz, M.; Scaiano, J. C.; Edwards, A. M.; Lissi, E. Photophysical Behaviour and Photodynamic Activity of Zinc Phthalocyanines Associated to Liposomes. *Photochem. Photobiol. Sci.* **2011**, *10*, 507−514.
(40) Li, D. S.; Yoon, S. J.; Pelivanov, I.; Frenz, M.; O'Donnell, M.; Pozzo, L. D. Polypyrrole-Coated Perfluorocarbon Nanoemulsions as a Sono-Photoacoustic Contrast Agent. *Nano Lett.* **2017**, *17*, 6184−6194.
(41) Song, G.; Liang, C.; Yi, X.; Zhao, Q.; Cheng, L.; Yang, K.; Liu, Z. Perfluorocarbon-Loaded Hollow Bi_2Se_3 Nanoparticles for Timely Supply of Oxygen under Near-Infrared Light to Enhance the Radiotherapy of Cancer. *Adv. Mater.* **2016**, *28*, 2716−2723.
(42) Mitragotri, S. Healing Sound: the Use of Ultrasound in Drug Delivery and Other Therapeutic Applications. *Nat. Rev. Drug Discovery* **2005**, *4*, 255−260.
(43) Ho, Y. J.; Chang, Y. C.; Yeh, C. K. Improving Nanoparticle Penetration in Tumors by Vascular Disruption with Acoustic Droplet Vaporization. *Theranostics* **2016**, *6*, 392−403.
(44) Tang, W.; Zhen, Z.; Wang, M.; Wang, H.; Chuang, Y.-J.; Zhang, W.; Wang, G. D.; Todd, T.; Cowger, T.; Chen, H.; Liu, L.; Li, Z.; Xie, J. Red Blood Cell-Facilitated Photodynamic Therapy for Cancer Treatment. *Adv. Funct. Mater.* **2016**, *26*, 1757−1768.
(45) Zhen, Z.; Tang, W.; Chen, H.; Lin, X.; Todd, T.; Wang, G.; Cowger, T.; Chen, X.; Xie, J. RGD-Modified Apoferritin Nanoparticles for Efficient Drug Delivery to Tumors. *ACS Nano* **2013**, *7*, 4830−4837.

DOI: 10.1021/acsnano.7b08628
ACS Nano 2018, 12, 2610−2622

(46) Baas, P.; van Mansom, I.; van Tinteren, H.; Stewart, F. A.; van Zandwijk, N. Effect of N-Acetylcysteine on Photofrin-Induced Skin Photosensitivity in Patients. *Lasers Surg. Med.* **1995**, *16*, 359−367.
(47) Zhen, Z.; Tang, W.; Guo, C.; Chen, H.; Lin, X.; Liu, G.; Fei, B.; Chen, X.; Xu, B.; Xie, J. Ferritin Nanocages to Encapsulate and Deliver Photosensitizers for Efficient Photodynamic Therapy against Cancer. *ACS Nano* **2013**, *7*, 6988−6996.
(48) Sano, K.; Nakajima, T.; Choyke, P. L.; Kobayashi, H. Markedly Enhanced Permeability and Retention Effects Induced by Photo-Immunotherapy of Tumors. *ACS Nano* **2013**, *7*, 717−724.
(49) Castano, A. P.; Mroz, P.; Hamblin, M. R. Photodynamic Therapy and Anti-Tumour Immunity. *Nat. Rev. Cancer* **2006**, *6*, 535−545.
(50) Lee, H. Y.; Kim, H. W.; Lee, J. H.; Oh, S. H. Controlling Oxygen Release from Hollow Microparticles for Prolonged Cell Survival under Hypoxic Environment. *Biomaterials* **2015**, *53*, 583−591.

DOI: 10.1021/acsnano.7b08628
ACS Nano 2018, 12, 2610−2622